JOM
https://doi.org/10.1007/s11837-024-06378-9

TECHNICAL ARTICLE

Mechanical Behavior of $Al_{0.5}$CoCrFeNi HEA During Warm Deformation

ARMIN GHADERI [1,2] and KAMRAN DEHGHANI [1,3]

1.—Department of Materials and Metallurgical Engineering, Amirkabir University of Technology, Tehran, Iran. 2.—e-mail: ghaderiarmin5@gmail.com. 3.—e-mail: dehghani@aut.ac.ir

The serrated flow during tensile testing of $Al_{0.5}$CoCrFeNi high-entropy alloy at 200–500°C and strain rates of 10^{-2}–10^{-4} s^{-1} was evaluated in this study. The temperature range of serration flow in the stress-strain curve changed as the strain rate increased. In addition, due to increased temperature and chromium enrichment of phase B2, the strength was considerably improved. Conversely, at 400–500°C, the elongation was significantly reduced while the strength increased from 300 MPa to 500 MPa to approximately 800 MPa. These changes were attributed to the precipitation of phase B2 and the enrichment of the B2 phase with Cr.

INTRODUCTION

High-entropy alloys (HEAs) belong to the category of advanced materials that emerged in the early years of this century.[1,2] Developing new kinds of new types of alloys with an equiatomic or near-equiatomic composition is now possible.[3,4] The HEAs are composed of at least five elements with identical or comparable atomic percentages.

Most HEAs exhibit typical phases such as face-centered cubic (FCC), body-centered cubic (BCC), or hexagonally closed packed (HCP).[5–15] Each element in the HEAs can be considered a solute, representing a dissolved substance. As a result, the solute atom concentration in HEAs is typically higher than in conventional alloys.[16,17] It is widely accepted that any atom can function as a solute atom in HEAs.[1] In certain instances, dislocation locking may be possible only if the matrix contains particular atoms. Numerous solid solutions exhibit a phenomenon known as the Portevin–Le Chatelier (PLC) effect when subjected to various temperatures and strain rates.[18–22]

Serrations often appear on stress-strain curves. Typically, the serration behavior of dislocations can be explained in terms of their interaction with diffusing atoms in the solute. Recent reports indicate that HEAs are characterized by serrated flows.[5,18–28] According to the characteristics of the flow, the serrated flow has been classified into three categories: A, B, and C.[28,29]

Notably, types A and B serrations are created through the pinning process, in which solvents gather to pin moving dislocations. In either case, there is a similar increase in stress until the dislocations separate from the solvent, after which the stress decreases rapidly because of the unpinning effect. However, type B serration oscillates at a higher frequency than type A. Generally, type C begins with a procedure involving unpinning.[29]

Multiple studies of serrated flow in conventional alloys were conducted to confirm the critical strain's temperature and strain rate dependence in a serrated flow. These studies indicate that the evaluation of activation energy for serrated flow is crucial for understanding the underlying mechanism, which should determine the nature of the solutes responsible for pinning or unpinning. It has been proposed that discrete substitutional solutes, such as molybdenum and chromium, and interstitial atoms, such as carbon and nitrogen, may interact with moving dislocations in conventional alloys. Only certain additives, such as Al, can inhibit the motion of dislocations in deformed HEAs, according to studies.[29–31]

Yasuda et al.[32] studied the mechanical properties of $Al_{0.3}$CoCrFeNi and the dynamic strain aging (DSA) characteristics of CoCrFeNi HEAs. According to their findings, the Al-containing HEAs possessed serrations, whereas the CoCrFeNi HEA lacked

---

(Received May 20, 2023; accepted January 5, 2024)

these characteristics concerning DSA. It was hypothesized that in the presence of Al solutes, the increase of pressure on the dislocations would lead to the evolution of serrations in the stress strain. Due to the interaction between carbon impurities and dislocations, the presence of carbon impurities and the stacking fault energy of carbon-doped CoCrFeMnNi HEAs led to the formation of serrated flows at room temperature (RT).[33]

In a recent study, Tong et al.[20] observed serrated flow in the stress-strain curve of $Al_{0.5}CoCrCuFeNi$ under compression; this occurred at high temperatures of 573–973 K and strain rates of 10^{-3} s^{-1}. In addition to solute atoms, dislocation-locking processes in HEAs can also involve nanoparticles and structural phases. Chen et al.[34] demonstrated that $Al_{0.5}CoCrCuFeNi$ HEA provides a barrier for mobile dislocations during compression when $L1_2$ particles are present. In another study, it was proposed that sigma-phase particles and dendrite boundaries could be used to inhibit dislocation motion, resulting in serrated stress-strain curves.[35]

Consequently, this study aimed to investigate the serration behavior of the $Al_{0.5}CoCrFeNi$ HEA under consideration, the effect of temperature and strain rate on the stress-strain curve of CoCrFeNi HEA, and the effect of both variables. Furthermore, the influence of Cr-rich precipitations on the mechanical properties of the alloy, particularly their effect on the stress-strain curves in specific temperature ranges, was examined, an additional important aspect of the present study.

MATERIALS AND METHODS

HEA ingots with nominal compositions of $Al_{0.5}CoCrFeNi$ were produced using the vacuum arc melting (VAR) technique in an inert atmosphere (argon). Each element had a minimum purity of 99.5 wt.%. At least five cycles of melting and solidification were required to achieve the desired level of alloy homogeneity. The molten alloy was then poured into a 12 mm × 25 mm × 140 mm copper mold. To compensate for the loss of Al through evaporation due to its relatively high vapor pressure, a proportionally high volume of Al (10 wt.%) was added to each ingot. The ingot was homogenized at 1100°C for 24 h in an argon atmosphere and then furnace cooled to room temperature. The composition of the produced alloy, as determined by an XRF machine (X Unique II, Philips), is shown in Table I. This corresponds to the nominal composition of $Al_{0.5}CoCrFeNi$.

Table I. Chemical composition of studied $Al_{0.5}CoCrFeNi$ high-entropy alloy

Element	Al	Co	Cr	Fe	Ni
at.%	11.23	22.18	22.23	22.21	22.15

Crystallographic analysis was performed using a Rigaku Ultima IV X-ray diffractometer equipped with $Cu_{K\alpha}$ (λ = 0.154056 nm) radiation at 40 kV and 30 mA. In this study, the microstructure and fracture surfaces of the samples were examined using a scanning electron microscope (SEM) (VEGA-II, Tescan) and energy-dispersive spectroscopy (EDS). The tensile strength was determined using flat dog-bone-shaped samples with a gauge length of 6.9 mm and a thickness of 1 mm, as shown in supplementary Fig. S-1. For the measurement of the tensile properties of the material, the extensometer was used. A Shimadzu AG-25TC testing machine was used for tensile testing at high temperatures (200–500°C) and heating rate 20°C/min and strain rates of 10^{-2} s^{-1}, 10^{-3} s^{-1}, 5×10^{-4} s^{-1}, and 10^{-4} s^{-1}.

RESULTS AND DISCUSSION

Microstructural Evolution

Figure 1 depicts the XRD patterns of $Al_{0.5}CoCrFeNi$ HEA taken from the as-cast and homogenized structures. As indicated by the diffraction peaks' relative intensities, both states' crystalline structure exhibits a mixture of FCC and BCC phases, with FCC being the predominant phase. As a result of homogenization, the intensity of the FCC peak decreased while the intensity of the BCC peak increased, indicating that some FCC phases had transitioned into BCC phases. Figure 2 illustrates the microstructures of both the as-cast and homogenized specimens, while Table II summarizes the chemical compositions of the various phases. The as-cast alloy exhibits typical dendritic (DR) and inter-dendritic (ID) structures,[36] as shown in Fig. 2a. Consequently, it is evident that the DR structures correspond to the different FCC phases,

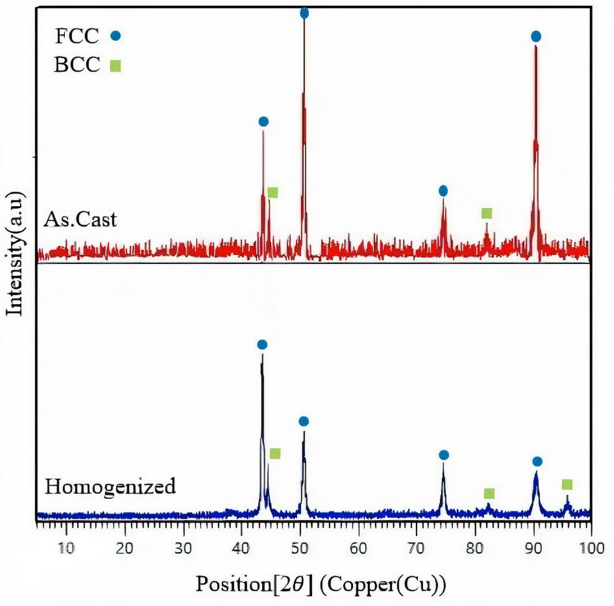

Fig. 1. X-ray diffraction (XRD) patterns of as-cast and homogenized $Al_{0.5}CoCrFeNi$ HEAs.

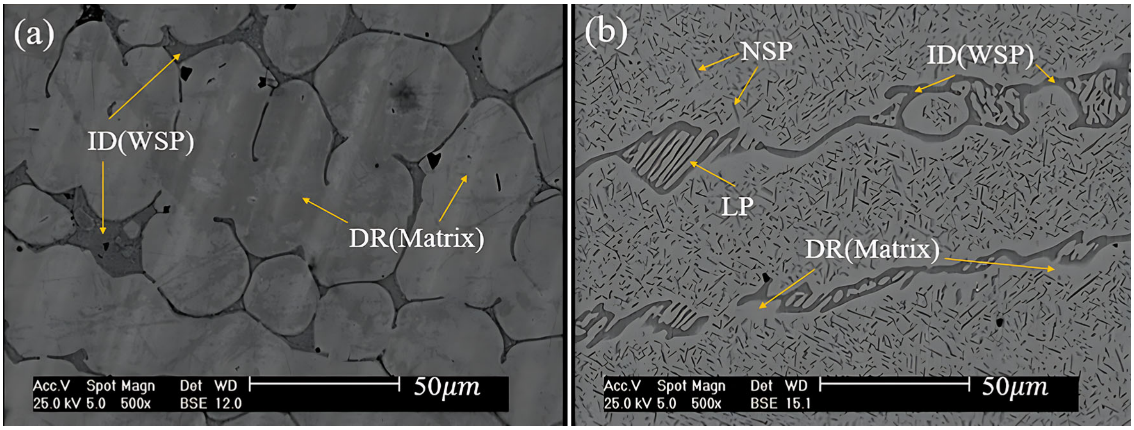

Fig. 2. SEM images of the $Al_{0.5}$CoCrFeNi alloy microstructure: (a) as-cast, (b) homogenized at 1100°C for 24 h.

Table II. EDS results of phases in as-cast and homogenized states

Elements	Al	Co	Cr	Ni	Fe
As-cast					
DR (matrix)	10.23	22.85	22.77	23.11	21.04
ID (DSP)	24.76	19.24	14.21	14.15	27.64
Homogenized					
DR (matrix)	9.54	23.71	21.28	22.26	23.21
ID (DSP)	25.74	18.18	14.18	13.29	28.61
WSP	15.17	20.86	23.73	21.83	18.42
NSP	18.72	20.12	19.26	20.74	21.16

while the ID structures correspond to the different BCC phases. In addition, it was observed that the inter-dendritic phase exhibited three distinct forms: wall-shaped phase (WSP), lamellar phase (LP), and needle-shaped phase (NSP). After homogenization, several of these ID regions dissolved into the matrix as their form changed from a continuous net phase to a wall-shaped phase distinct from the continuous phase.

Samples contain a preponderance of dendrites and a moderate number of interdendritic regions, as evidenced by SEM observations. However, relatively few inter-dendritic regions are present in the collected sample. SEM micrographs and elemental distribution of various phases of the $Al_{0.5}$CoCrFeNi alloy were established in two distinct states, as shown in Table II and Fig. 2. Based on the results for all specimens, Fe, Cr, Co, and Ni were identified as the major elements in the matrix, whereas Al-Ni was identified as the predominant element in the WSP. In addition, NSP phases, which appear to expand after the matrix and reach the as-cast state, were rich in Cr, Ni, Co, Al, and Fe, whereas LP phases were typically rich in Cr, Co, and Fe but deficient in Al-Ni. Furthermore, Al and Ni typically segregate toward the ID of the casting when the alloy is cast. Al has the largest atom radius of the five elements, and Al-Ni has the highest mixing enthalpy, which can be explained by Al having the largest atom radius.[37]

Serrated Flow Behavior

In engineering stress-strain curves, pronounced serrated flow behaviors frequently extend to the yield points in the HEA, as shown by the partially enlarged segments in supplementary Fig. S-2. Existing theories and models classify serrated flows into three types, A, B, and C, based on the types observed in existing data. This can be explained as the pinning of dislocations by stress increment; in general, solutes gather around dislocations and render them immobile during the pinning process. Dislocations can break away from these solutes, however, when a certain threshold of local stress is exceeded, causing a sudden drop in local pressure during the unpinning process, which can result in the dislocation breaking away.[38] Since type B serrations appear at higher temperatures than type A serrations, the solute atom diffuses more quickly and effectively, resulting in more effective pinning at higher temperatures.[38] This leads to a more continuous serration pattern in type B as the serrations are larger and continuous.[38]

In contrast, type C serrations are formed by an unpinning process that occurs during the formation of the serrations, and discontinuous serrations result from dislocations' ability to move with solutes while remaining adhered to these pinning atoms as the temperature further rises.[39] The serrations of type D indicate that there are some continuous steps. Type E displays arbitrary behavior.[40]

When plastic deformation takes place in a variety of materials, serrated flow can occur because of the following mechanisms: (1) martensitic transformation; (2) deformation twinning; (3) the interaction between the solute atoms and dislocation (DSA).[41]

Notably, the experiment did not appear to show strain-induced phase transformation. It would therefore seem unlikely that the strain-induced transformation of $Al_{0.5}$CoCrFeNi HEA would result in serrated flow as a result of serrated flow.[41]

The phenomenon of serration, in general, can be identified as the result of the DSA, that is, the interaction between the dislocation and the solute atom. McCormick[42] has suggested that when dislocations are impeded by obstacles during the process of plastic deformation, the solute atoms diffuse to the area surrounding the dislocations when they are impeded by obstacles. At the same time, thermal activation is causing the dislocations to wait to be released. This is called the critical waiting time if the waiting period is long enough for the solute atoms to diffuse and pin the dislocations, which is also known as the aging time. There is a shorter waiting time than the aging time at the beginning of the tensile stress-strain curve. This results in smooth curves because of this process. With an increase in strain, there is also an increase in dislocation density, resulting in a significant increase in waiting times. Additionally, as the vacancy concentration increases from the plastic deformation, the diffusion of solute atoms is accelerated, resulting in a shorter aging time and a smaller gap due to the shorter aging time. Notably, the serrations appear when the two times are equal. There is a decreasing diffusion rate of solute atoms when the temperature is decreased, which naturally results in a longer aging time for the solution. A relatively long waiting time and a high vacancy concentration are needed, both of which can be achieved by increasing strain. This is what causes the critical strain to increase with the decrease in temperature.[42]

Four distinct stress-strain curves are shown in Figs. 3, 4, 5 and 6 that correspond to temperatures between 200°C and 500°C and strain rates between 10^{-2} s^{-1} to 5×10^{-4} s^{-1}. As shown in these figures, the segments of the serrations can be observed in greater detail so that the type of serration can be better understood. Serrations tend to form in the temperature range of 300–500°C for strain rates of 10^{-2} s^{-1} to 5×10^{-4} s^{-1} and 200–400°C for a strain rate 10^{-4} s^{-1}.

The strain rate of 10^{-2} s^{-1} between 300°C and 500°C indicates that this is of the type E $\rightarrow$ E $\rightarrow$ C (Fig. 3). In terms of serration, the strain rate of 10^{-3} s^{-1} evolves a type A + B serration at 300°C, followed by a type B + C serration at 400°C and a type C serration at 500°C. Despite this, the type A + B $\rightarrow$ B $\rightarrow$ C transformation is observed at a strain rate of 5×10^{-4} s^{-1} at temperatures comparable to 10^{-3} s^{-1}. At 300°C, the serration evolves at a strain rate of 10^{-4} s^{-1} into the E + B type, the B + C type, and, finally, the B + C type at 500°C. Figure 7 depicts the relationship between serration type, temperature, and strain rate. This relationship demonstrates that, in response to an increase in temperature and a decrease in strain rate, serration type will evolve from type A to type A + B or E to type B + C and eventually evolve into type B + C.

Formation of Intermetallic Cr-rich Precipitations

Studies indicate that the phase is stable between 350–720°C, 350–810°C, and 350–900°C for the $Al_{0.3}$CoCrFeNi, $Al_{0.5}$CoCrFeNi, and $Al_{0.7}$CoCrFeNi contents, respectively.[43] In each of these three types of HEAs, the σ phase exists. This is because (1) it has also been demonstrated that the σ phase forms in binary systems such as Cr-Co, Cr-Fe, and Cr-Ni; (2) the phase of HEAs is not intrinsically unstable for substitutional elements (such as Al, Co, Cr, Fe, and Ni) because of their similar atomic radii.[43]

The Cr-rich phases were only observed in the B2 region in $Al_{0.5}$CoCrFeNi, which can be explained as follows: (1) There is a Cr-rich phase, the second phase of a substitution-rich element. Their slow diffusion during the FCC phase significantly affects the diffusion of substitutional elements.[42] Because the FCC phase contains a Cr-rich phase, it is challenging to nucleate the phase. (2) The interface between the Cr-rich and FCC phases is incoherent. Thus, the Cr-rich structure cannot form during the FCC phase.[45–48]

σ-phase precipitation can form in three steps for $Al_{0.5}$; (1) this Cr-rich BCC phase nucleates within the B2 (inter-dendritic) region because of the coherent interfaces and concentration profiles that determine the distribution of Cr in the B2(ID) region; (2) the initiation of the phase occurs at the interface of the BCC and B2(ID) phases and rapid growth within the BCC phase, which is calculated based on the pattern of Cr-concentration profiles (partitioning of alloying elements); (3) the remaining BCC phase is currently at the eutectic decomposition around 600°C.[46] Additionally, at high temperatures in the $Al_{0.7}$ region, the phase can directly form the FCC matrix.[46]

The globular shape of the σ phase within the matrix demonstrates the absence of a relationship between the σ phase and the FCC matrix.[43,45] The calculated temperature at which the phase forms in $Al_{0.3}$, $Al_{0.5}$ and $Al_{0.7}$ HEAs implies that the σ phase will be able to withstand higher temperatures as the Al ratio of alloys increases, which correlates with an increase in hardness and a decrease in elongation as the Al ratio of HEAs increases.[43]

Based on SEM images (Fig. 8), the presence of the Cr-rich phase can be observed in specimens assessed at various strain rates and temperatures. This is due to increased strength and decreased elongation during the formation of the Cr-rich phase. When a strain rate of 10^{-3} s^{-1} is applied at 300°C, a matrix with an FCC structure rich in Cr and Fe is formed. In addition, the droplet phase with an FCC structure is rich in the Cr- and Fe-

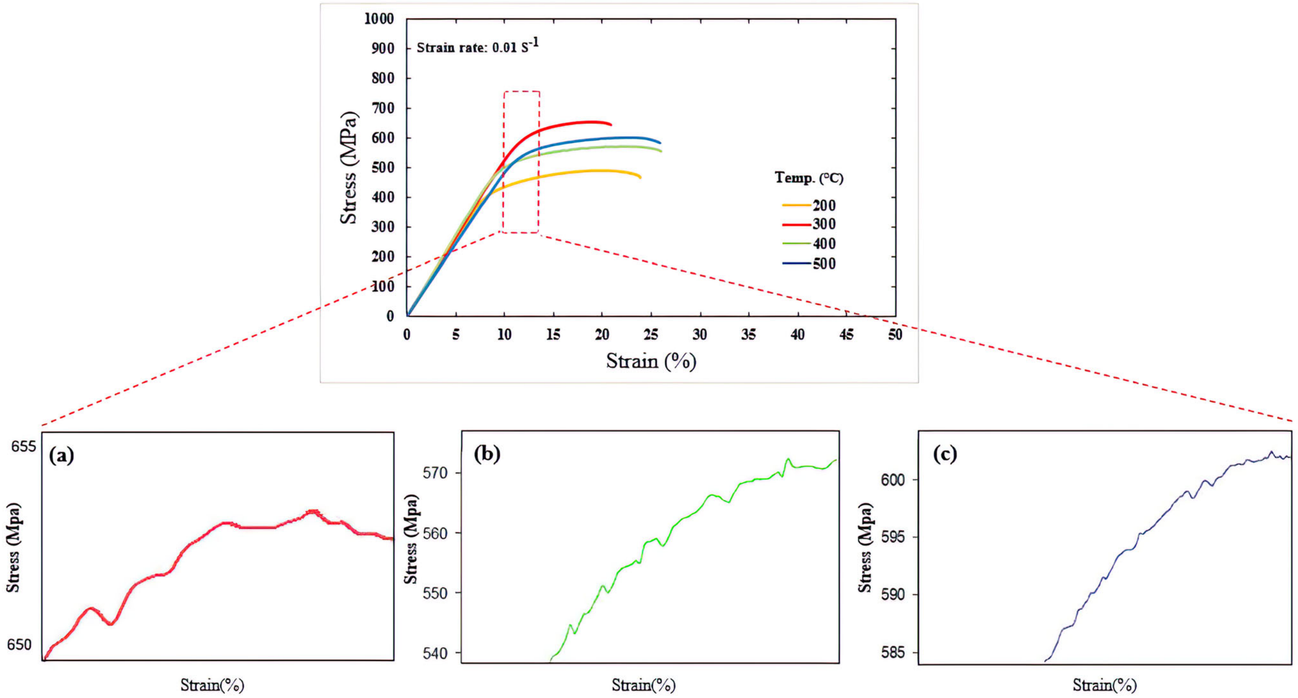

Fig. 3. Tensile true stress–strain curve of the heat-treated $Al_{0.5}$CoCrFeNi alloy with a strain rate 10^{-2} s^{-1} at different temperatures and a magnified portion of stress-strain curves with serration types for (a) 300°C, (b) 400°C, (c) 500°C.

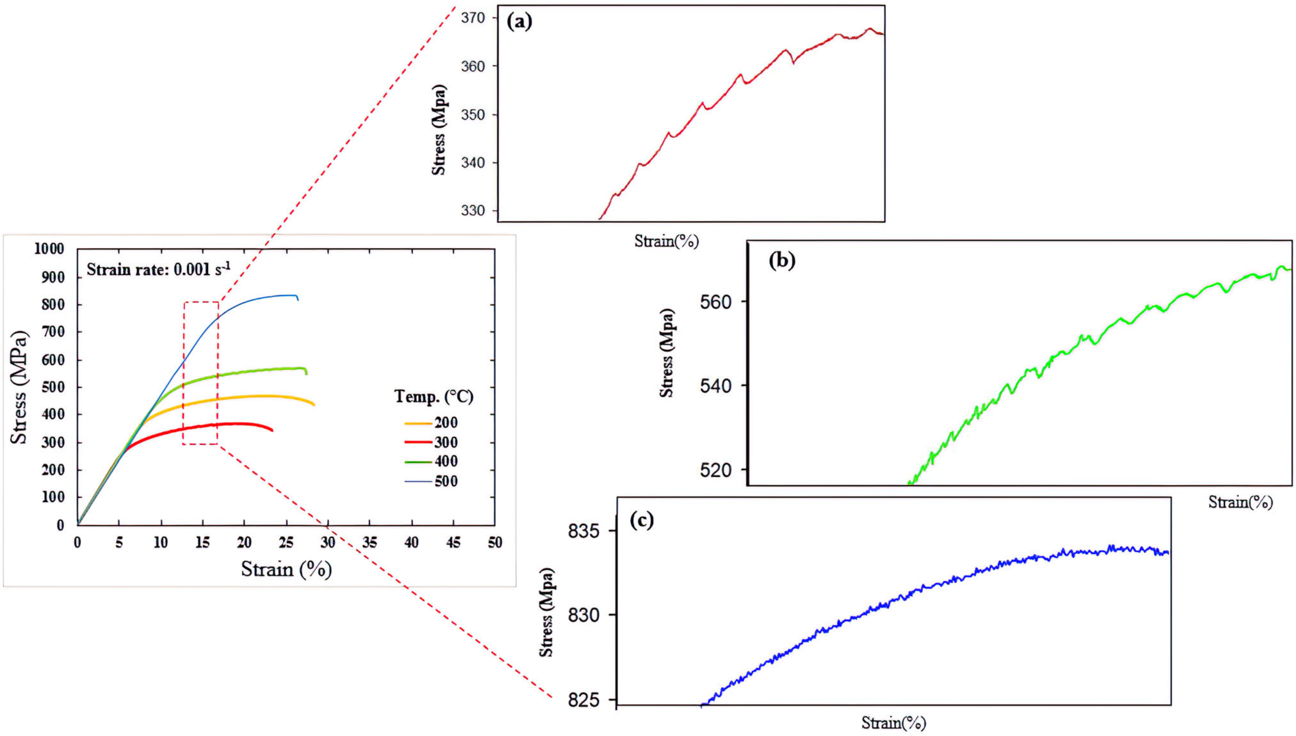

Fig. 4. Tensile true stress-strain curve of the heat-treated $Al_{0.5}$CoCrFeNi alloy with a strain rate 10^{-3} s^{-1} at different temperatures and a magnified portion of stress-strain curves with serration types for (a) 300°C, (b) 400°C, (c) 500°C.

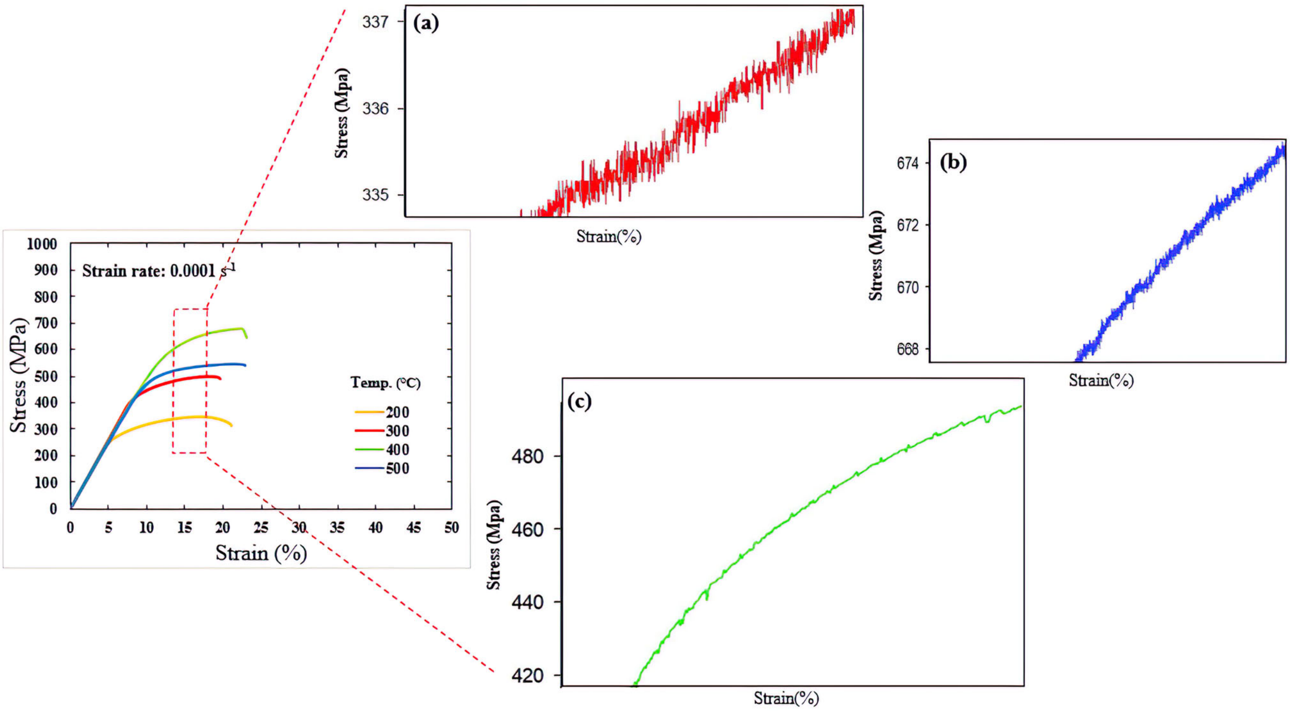

Fig. 5. Tensile true stress-strain curve of the heat-treated $Al_{0.5}CoCrFeNi$ alloy with strain rate 10^{-4} s^{-1} at different temperatures and a magnified portion of stress-strain curves with serration types for (a) 200°C, (b) 300°C, (c) 400°C.

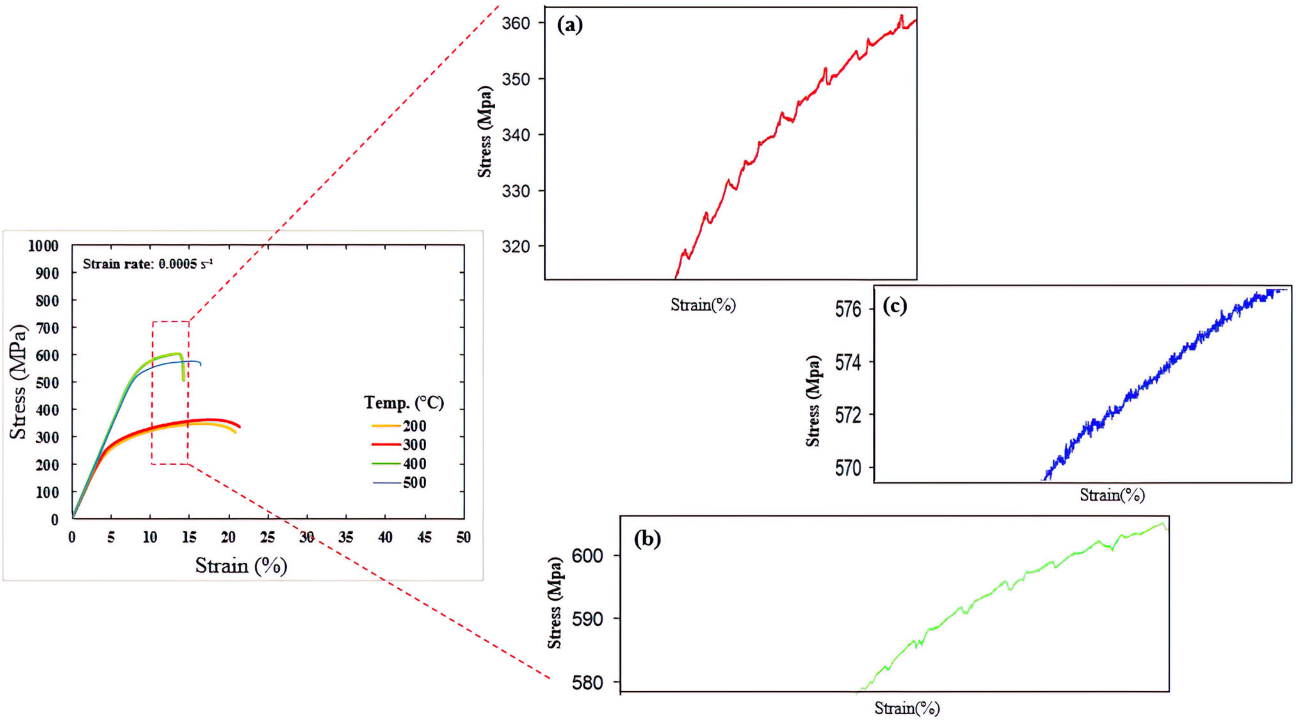

Fig. 6. Tensile true stress-strain curve of the heat-treated $Al_{0.5}CoCrFeNi$ alloy with strain rate 5×10^{-4} s^{-1} at different temperatures and a magnified portion of stress-strain curves with serration types for (a) 300°C, (b) 400°C, (c) 500°C.

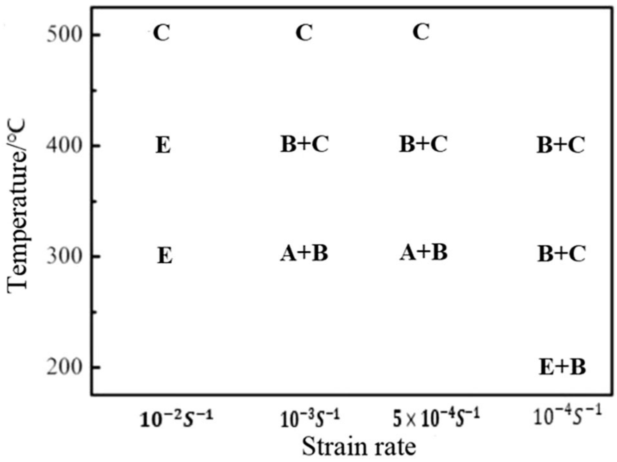

Fig. 7. Schematic of serration types concerning strain rate and temperature.

depleted Al-Ni phases. This is accompanied by the BCC-structured precipitation of spherical Al-(Ni-Co-Cr-Fe) B2 in the matrix.

According to backscatter electron (BSE) images and EDX maps of all matrix phases, the distribution of the element Co is nearly uniform across all samples. At temperatures between 400°C and 500°C, the Cr-rich phase constitutes a significant portion of the matrix. The needle-shaped Cr-rich phase nucleates at the interface between the B_2 phase and the matrix. In addition, an increase in temperature results in a rise in the volumetric fraction of Cr-rich phases. The maximum Cr-rich phase value can be obtained at a strain rate of 10^{-3} s^{-1} and a temperature of 500°C. According to the stress-strain diagram (Fig. 4), the presence of a maximum Cr-rich phase at the applied temperatures decreases elongation.

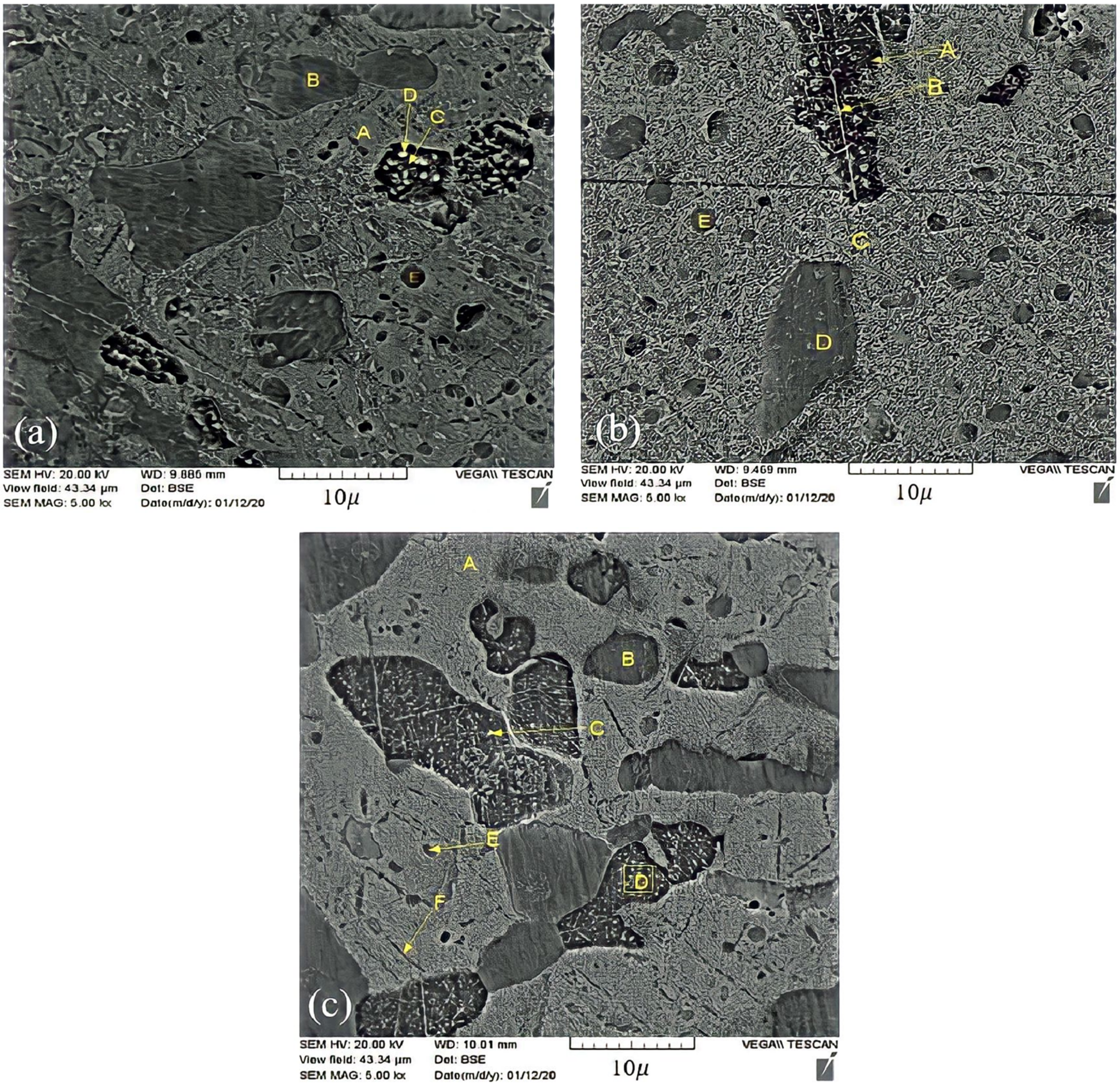

Fig. 8. BSE image of the $Al_{0.5}$CoCrFeNi alloy with a strain rate of 10^{-3} s^{-1} at temperatures of (a) 300°C, (b) 400°C, (c) 500°C.

The EDS analysis (Fig. 8) reveals that the enrichment of the B2 phase with Cr and the diffusion of Al into the matrix are additional causes for the change in the mechanical properties of the alloy at the strain rate of 10^{-3} s^{-1}. This also suggests that Al diffusion can form the B2 phase and a brittle matrix. An intriguing observation is that the spherical phase (light phase) inside the droplet phase, which is rich in nickel, nucleates as the droplet phase's temperature rises, resulting in the diffusion of nickel from the droplet phase into the spherical phase (light phase).

The spherical phase, indicated by point E in Fig. 8a and b, was depleted of chromium at 300°C. The phase becomes enriched with chromium when the temperature is raised to 400°C and thus the mechanical properties of this phase are increased. Furthermore, when the temperature is increased up to 500°C, the morphology of the B2 phase enriched with Cr changes from a spherical to a needle-shaped one, and this has a significant impact on the increase in strength of the alloy.

According to EDS analysis (Fig. 8 and supplementary Fig. S-3 and Table III), the Cr-rich phase, which is rich in Cr, is formed as a needle-like structure at the interface between phase B2 and the matrix. As previously stated, this phase is brittle and detrimental to mechanical properties. In this regard, it has a significant effect on the properties of the alloy. At 500°C, the formation of the σ phase alters the material's mechanical properties, as shown by the stress-strain diagram at a strain rate of 10^{-3} s^{-1}. In addition, the transformation of phase B2 into a brittle phase, the enrichment of this phase with Cr, and the internal diffusion within the matrix are the factors that influence the appearance of the stress-strain curve in terms of serrations (Fig. 4).

Effect of the Cr-rich Phase on Hardness

The hardness tests conducted on tensile specimens at various strain rates and temperatures (Fig. 9) indicate that the specimens' hardness increases in the gauge section.

Regarding the strain rate of 10^{-3} s^{-1}, as discussed previously, the serration flow appears at approximately 300°C and persists up to approximately 500°C, which is consistent with the hardness results (Fig. 9). Along with the increase in the specimens' hardness, the temperature at which the serration flow appears rose by a significant amount. Another indicator of serration behavior during tensile testing is the discernible increase in specimen hardness. A similar increase in hardness was observed across the strain rates and serration flow spectrum. Since the increase in hardness due to the formation of chromium-rich phase is the same in all parts of a sample and cannot justify the significant difference in hardness in Fig. 9, chromium-rich deposits certainly contribute to increased hardness. The increase in hardness may result from a complex interplay between strain hardening due to previous plastic deformation, partial destruction of recovery, and nucleation of new phases but the significant difference in the hardness value between the gauge

Table III. EDS analysis results of the sample with a strain rate of 10^{-3} s^{-1} at 300°C, 400°C, and 500°C concerning chemical composition (%)

Temperature (°C)	Unit (%)	Al	Co	Cr	Fe	Ni
300	A	4.06	25.42	24.18	25.97	20.37
	B	19.68	20.36	11.32	15.07	33.58
	C	19.91	18.42	7.48	13	41.19
	D	25.77	17.91	7.10	11.07	38.15
	E	19.09	20.58	11.25	14.84	34.23
400	A	8.56	23.60	17.96	21.37	28.51
	B	14.91	21.72	12.52	16.20	34.65
	C	5.76	25.52	22.49	24.53	21.70
	D	19.65	21.08	9.26	13.57	36.45
	E	5.42	25.33	22.31	25.02	21.92
500	A	4.43	26.46	23.96	24.87	20.28
	B	22.16	18.60	6.87	12.20	40.17
	C	22.55	18.66	11.12	13.47	34.21
	D	17.88	20.30	13.56	16.03	32.23
	E	12.39	22.29	19.37	20.63	25.33
	F	6.01	25.15	22.85	23.56	22.42

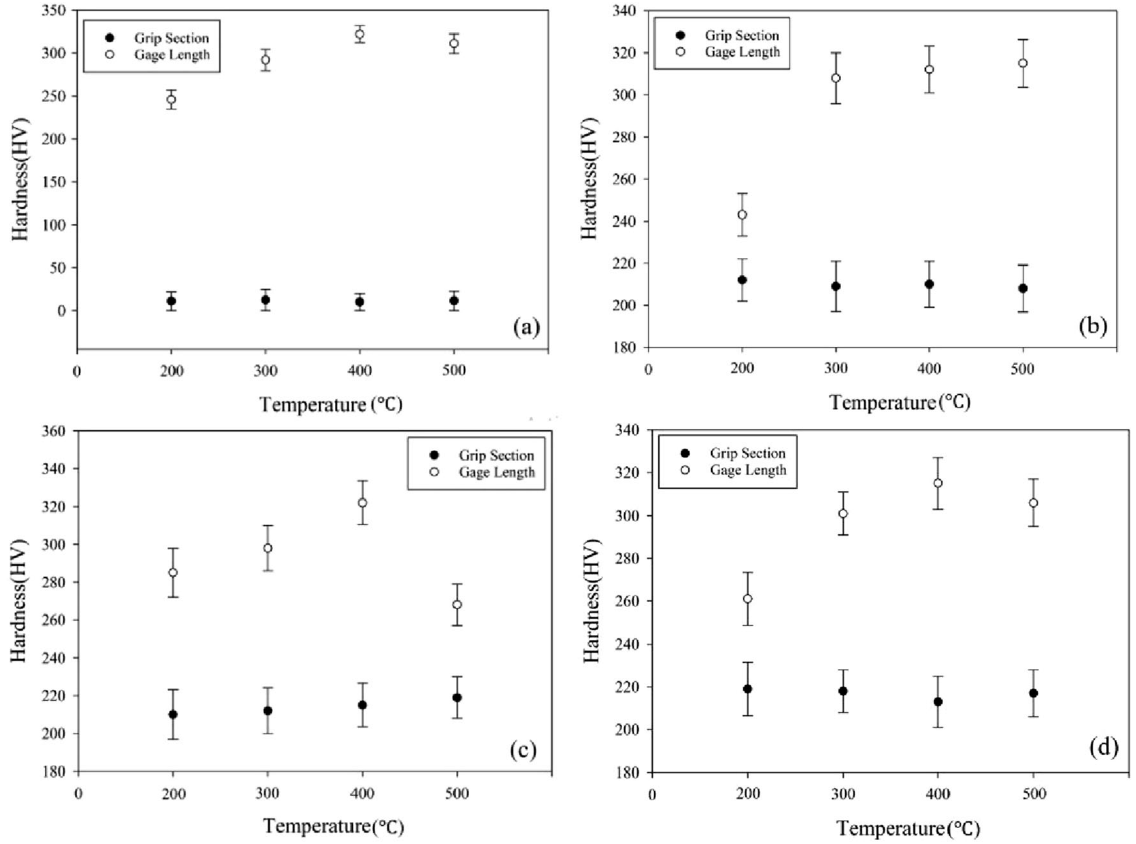

Fig. 9. Comparison of hardness and tensile tests performed on samples at different temperatures and strain rates: (a) 10^{-2} s^{-1}, (b) 10^{-3} s^{-1}, (c) $10^{-4}s^{-1}$, (d) 5×10^{-4} s^{-1}.

and grip part indicates the locking of dislocations by dissolved atoms, which is the main reason for the formation of DSA, which is the cause of the tremendous increase in hardness caused by the serration phenomenon.

Fractography of Tensile Samples

Figure 10 depicts the typical fracture surfaces of samples investigated at various temperatures and strain rates of 10^{-3} s^{-1}. All specimens exhibit a typical dimple morphology, indicating that the specimens underwent significant plastic deformation and failed in a ductile fracture mode. Clearly, there are no indications of brittle fracture. The mechanism of fracture is trans-granular ductile fracture. At 300°C, the dimples are relatively larger but shallow, and their elongation is moderate. In contrast, at 500°C, even though the dimples appear large, they appear deeper, which correlates with significant elongation compared to 300°C. As for 400°C, there is an abundance of fine dimples representing considerable elongation.

CONCLUSION

In this study, the serrated flow of $Al_{0.5}$CoCrFeNi HEA at temperatures between 200°C and 500°C and strain rates between 10^{-3} s^{-1} and 5×10^{-4} s^{-1} was investigated. The well-established PLC phenomenon was observed under the studied condition. However, as the temperature increased and the strain rate decreased, the serration type shifted from type A to type A + B and then to type B + C. As the strain rate increased, the temperature range in which serration occurred also increased. In addition, the increase in strain rate caused type A serrations to transform into type E.

When annealing the high-entropy alloy $Al_{0.5}$CoCrFeNi at 300–500°C, the brittle phase of Cr-rich formed at the interface of phase B2 and matrix phase, increasing the material's strength

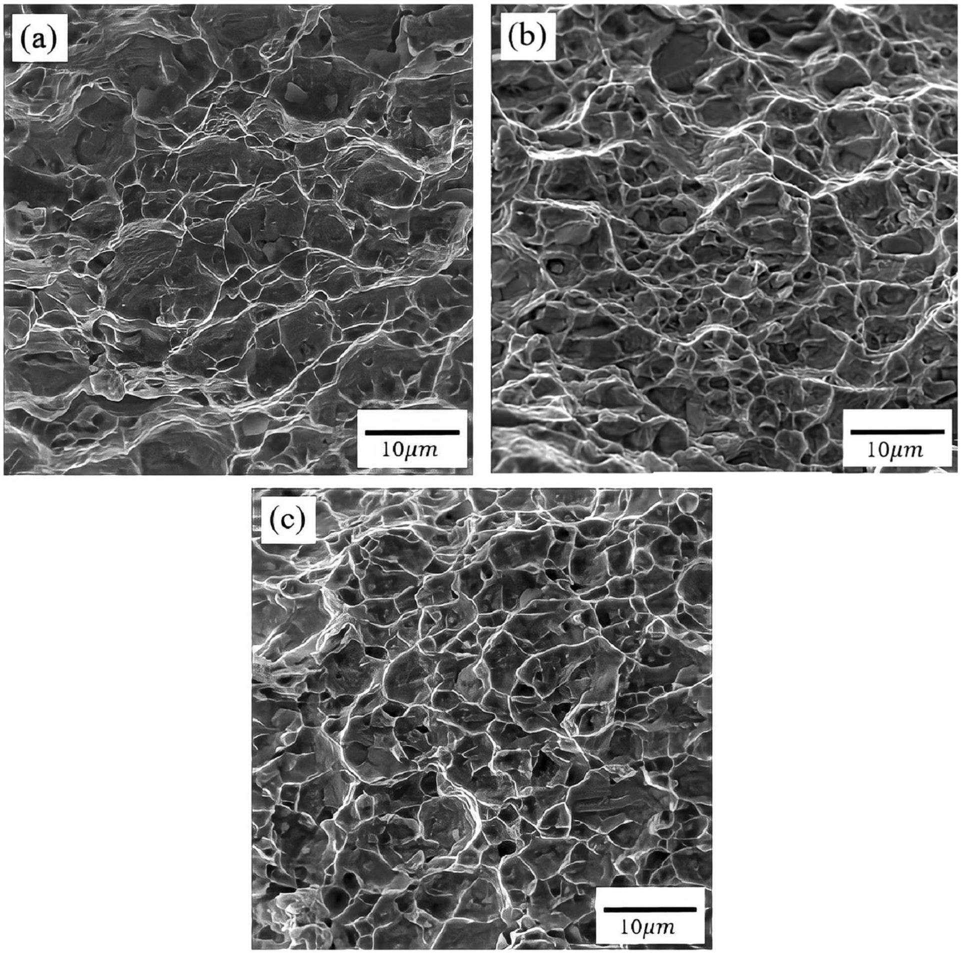

Fig. 10. SEM micrographs of the samples' fracture surfaces at a strain rate of 10^{-3} s^{-1} at different temperatures: (a) 300°C, (b) 400°C, (c) 500°C.

and decreasing its elongation. Similar evidence of the B2 phase enriched with Cr was observed between 300°C and 500°C.

The relationship among serration type, temperature, and strain rate demonstrates that the serration type will evolve from type A to type A + B or E to type B + C because of rising temperatures and decreasing strain rates and will eventually evolve into type B + C because of rising temperatures and decreasing strain rates.

SUPPLEMENTARY INFORMATION

The online version contains supplementary material available at https://doi.org/10.1007/s11837-024-06378-9.

CONFLICT OF INTEREST

On behalf of all authors, the corresponding author states that there is no conflict of interest.

REFERENCES

1. J.W. Yeh, S.J. Lin, T.S. Chin, J.Y. Gan, S.K. Chen, T.T. Shun, C.H. Tsau, and S.Y. Chou, *Metall. Mater. Trans. A* 35, 2533–2536 (2004).
2. J.W. Yeh, S.K. Chen, S.J. Lin, J.Y. Gan, T.S. Chin, T.T. Shun, C.H. Tsau, and S.Y. Chang, *Adv. Eng. Mater.* 6(5), 299–303 (2004).
3. Y. Zhang, Y.J. Zhou, J.P. Lin, G.L. Chen, and P.K. Liaw, *Adv. Eng. Mater.* 10(6), 534–538 (2008).
4. R. Raghavan, K.C.H. Kumar, and B.S. Murty, *J. Alloys Compd.* 544(15), 152–158 (2012).
5. Y. Zhang, T.T. Zuo, Z. Tang, M.C. Gao, K.A. Dahmen, P.K. Liaw, and Z.P. Lu, *Prog. Mater. Sci.* 61, 1–93 (2014).
6. J. Antonaglia, X. Xie, Z. Tang, C.W. Tsai, J.W. Qiao, Y. Zhang, M.O. Laktionova, E.D. Tabachnikova, J.W. Yeh, O.N. Senkov, M.C. Gao, J.T. Uhl, P.K. Liaw, and K.A. Dahmen, *JOM* 66(10), 2002–2008 (2014).

7. M.A. Hemphill, T. Yuan, G.Y. Wang, J.W. Yeh, C.W. Tsai, A. Chuang, and P.K. Liaw, *Acta Mater.* 60(16), 5723–5734 (2012).
8. M. Gao, and D. Alman, *Entropy* 15(10), 4504–4519 (2013).
9. H. Moghanni, K. Dehghani, and A. Shafiei, *J. Mater. Res. Technol.* 16, 1069–1089 (2022).
10. M.H. Tsai, and J.W. Yeh, *Mater. Res. Lett.* 874, 1–17 (2014).
11. Z. Wu, H. Bei, G.M. Pharr, and E.P. George, *Acta Mater.* 81, 428–441 (2014).
12. A. Ghaderi, H. Moghanni, and K. Dehghani, *J. Mater. Eng. Perform.* 30, 1–9 (2021).
13. K.M. Youssef, A.J. Zaddach, C. Niu, D.L. Irving, and C.C. Koch, *Mater. Res. Lett.* 3(2), 95–99 (2014).
14. L.J. Santodonato, Y. Zhang, M. Feygenson, C.M. Parish, M.C. Gao, R.J. Weber, J.C. Neuefeind, Z. Tang, and P.K. Liaw, *Nat. Commun.* 6, 5964 (2015).
15. Z. Tang, T. Yuan, C.W. Tsai, J.W. Yeh, C.D. Lundin, and P.K. Liaw, *Acta Mater.* 99, 247–258 (2015).
16. B. Cantor, I.T.H. Chang, P. Knight, and A.J.B. Vincent, *Mater. Sci. Eng. A* 375–377, 213–218 (2004).
17. Y. Zhou, D. Zhou, X. Jin, L. Zhang, X. Du and B. Li, *Sci. Rep.* **8**, Article number: 1236 (2018).
18. K. Zhang, and Z. Fu, *Intermetallics* 28, 34–39 (2012).
19. S. Chen, L. Yu, J. Ren, X. Xie, X. Li, Y. Xu, G. Zhao, P. Li, F. Yang, Y. Ren, and P.K. Liaw, *Sci. Rep.* 6, 29798 (2016).
20. C.J. Tong, Y.L. Chen, J.W. Yeh, S.J. Lin, S.-K. Chen, T.T. Shun, C.H. Tsau, and S.Y. Chang, *Metall. Mater. Trans. A* 36A, 881–893 (2005).
21. E. Pink, *Acta Metall.* 37(7), 1773–1781 (1989).
22. S.Y. Chen, X. Yang, K. Dahmen, P.K. Liaw, and Y. Zhang, *Entropy* 16(2), 870–884 (2014).
23. S.Y. Chen, X. Xie, B.L. Chen, J.W. Qiao, Y. Zhang, Y. Ren, K.A. Dahmen, and P.K. Liaw, *JOM* 67(10), 2314–2320 (2015).
24. H.Y. Diao, R. Feng, K.A. Dahmen, and P.K. Liaw, *Curr. Opin. Solid State Mater. Sci.* 21(5), 252–266 (2017).
25. X.F. Wang, Y. Zhang, Y. Qiao, and G.L. Chen, *Intermetallics* 15(3), 357–362 (2007).
26. O.N. Senkov, G.B. Wilks, D.B. Miracle, C.P. Chuangd, and P.K. Liaw, *Intermetallics* 18, 1758–1765 (2010).
27. B. Gludovatz, A. Hohenwarter, D. Catoor, E.H. Chang, E.P. George, and R.O. Ritchie, *Science* 345(6201), 1153–1158 (2014).
28. X.Y. Fang, D.Q. Yi, and J.F. Nie, *Metall. Mater. Trans. A* 40, 2761–2771 (2009).
29. S. Niu, H. Kou, Y. Zhang, J. Wang, and J. Li, *Mater. Sci. Eng. A Struct. Mater. Prop. Microstruct. Process.* 702, 96–103 (2017).
30. J. Brechtl, S.Y. Chen, X. Xie, Y. Ren, J.W. Qiao, P.K. Liaw, and S.J. Zinkle, *Int. J. Plast.* 115, 71–92 (2019).
31. M.S. Bijnavandi, A. Ghaderi, and K. Dehghani, *J. Mater. Eng. Perform.* 25, 1–8 (2023).
32. H.Y. Yasuda, K. Shigeno, and T. Nagase, *Scr. Mater.* 108, 80–83 (2015).
33. L. Guo, J. Gu, X. Gong, K. Li, S. Ni, Y. Liu, and M. Song, *Micron* 126, 102739 (2019).
34. S. Chen, X. Xie, W. Li, R. Feng, B. Chen, J. Qiao, Y. Ren, Y. Zhang, K.A. Dahmen, and P.K. Liaw, *Mater. Chem. Phys.* 210, 20–28 (2018).
35. E.D. Tabachnikova, A.V. Podolskiy, M.O. Laktionova, N.A. Bereznaia, M.A. Tikhonovsky, and A.S. Tortika, *Alloys Compd.* 698, 501–509 (2017).
36. C.M. Lin, and H.L. Tsai, *Intermetallics* 256, 288–294 (2011).
37. Z. Tang, M.C. Gao, H. Diao, T. Yang, J. Liu, T. Zuo, Y. Zhang, Z. Lu, Y. Cheng, Y. Zhang, K.A. Dahmen, P.K. Liaw, and T. Egami, *JOM* 65, 1848–1858 (2013).
38. D. Wu, R.S. Chen, and E.H. Han, *Mater. Sci. Eng. A* 532, 267–274 (2012).
39. Y. Cai, C. Tian, S. Fu, G. Han, C. Cui, and Q. Zhang, *Mater. Sci. Eng. A* 638(25), 314–321 (2015).
40. P. Rodriguez, *Bull. Mater. Sci.* 6, 653–663 (1984).
41. R.P. Singh, and R.D. Doherty, *Metall. Trans. A* 23, 321–334 (1992).
42. P.G. McCormick, *Acta Metall.* 20(3), 351–354 (1972).
43. J.C. Rao, H.Y. Diao, V. Ocelík, D. Vainchtein, C. Zhang, C. Kuo, Z. Tang, W. Guo, J.D. Poplawsky, Y. Zhou, P.K. Liaw, and JTh.M. De Hosson, *Acta Mater.* 131(1), 206–220 (2017).
44. C.C. Hsieh and W. Wu, *Int. Sch. Res. Not.* **2012**, Article ID 732471.
45. W.R. Wang, W.L. Wang, S.C. Wang, Y.C. Tsai, C.H. Lai, and J.W. Yeh, *Intermetallics* 26, 44–51 (2012).
46. E.J. Pickering, R. Muñoz-Moreno, H.J. Stone, and N.G. Jones, *Scr. Mater.* 113, 106–109 (2016).
47. F. Otto, A. Dlouhý, K.G. Pradeep, M. Kuběnová, D. Raabe, G. Eggeler, and E.P. George, *Acta Mater.* 112, 40–52 (2016).